PAPER

Check for updates

The effect of manganese oxidation state on antiferromagnetic order in SrMn₁₋ₓSbₓO₃ (0 < x < 0.5) perovskite solid solutions†

Gennady V. Bazuev,[a] Alexander P. Tyutyunnik, [ID][a] Alexander V. Korolev,[b] Emmanuelle Suard,[c] Cheuk-Wai Tai [ID][d] and Nadezda V. Tarakina [ID] *[ef]

The mixed-valence manganese (Mn^{3+}/Mn^{4+}) solid solution, $SrMn_{1-x}Sb_xO_3$, was prepared for the first time. Two ranges of solid solutions were found: (1) $SrMn_{1-x}Sb_xO_3$ ($0.025 \leq x \leq 0.09$) with monoclinically distorted 6H-$SrMnO_3$ polytype (sp. gr. $C/2c$) and (2) $SrMn_{1-x}Sb_xO_3$ ($0.17 \leq x \leq 0.50$) with a tetragonal unit cell (sp. gr. $I4/mcm$). Crystal structure refinement using X-ray and neutron powder diffraction data showed that the structure of the monoclinic solid solution consists of corner-sharing octahedra around sites occupied by manganese and antimony ions and face-sharing octahedra around sites occupied by manganese ions only, while the tetragonal solid solution has a random distribution of B-site cations. The presence of long-range antiferromagnetic order with a Néel temperature of about 148 K for $SrMn_{0.80}Sb_{0.20}O_3$ and about 280 K for $SrMn_{0.925}Sb_{0.075}O_3$ was found from the results of DC and AC susceptibility and neutron diffraction experiments at 5 K and 80 K.

Introduction

Manganites with perovskite-like structures attract considerable attention due to their unique electronic, magnetoelectrical and magnetic properties. Spontaneous electric polarization and magnetic ordering in the $Sr_{1-x}Ba_xMnO_3$ solid solution at $x \geq 0.45$,[1] ferromagnetic coupling and metallic conductivity in $La_{1-x}Ca_xMn_{4-x}Mn_{4+x}O_3$,[2] strong magnetoelectric effects near room temperature in single-crystal $BaMnO_{2.99}$ and its derivative $BaMn_{0.97}M_{0.03}O_3$ (M = Li or K),[3] soft ferromagnetic behaviour in $La_{0.75}K_{0.25}AMnTiO_6$ (A = Sr or Ba) at low-temperature,[4] collinear-magnetism-driven ferroelectricity in the Ising chains in Ca_3CoMnO_6[5,6] are just a few examples. Such variety of properties results from the interplay between charge, exchange and phonon interactions,[7] which can be adjusted by substituting either A-site cations or Mn with other cations (usually cations of

different sizes/charges). The latter influences the ratio of Mn cations in different oxidation states in the final compound and can also lead to the formation of different structural modifications within the perovskite type structure.

In this work we studied structural and magnetic properties of $SrMn^{4+}O_3$–$Sr_2Mn^{3+}SbO_6$ solid solutions. In order to explain why we chose to study this system, let's first look at the structure and properties of the two parent compounds $SrMnO_3$ and Sr_2MnSbO_6. They differ considerably in chemical composition, oxidation state of manganese, physical properties and their crystal structure.

Strontium manganite $SrMnO_3$ can be synthesised with three different modifications. $SrMnO_3$ produced at high temperatures and oxidized at 350 °C in air crystallises in an ideal cubic structure (sp. gr. $Pm\bar{3}m$, a = 3.8041(3) Å, $Z = 1$[8]), with Sr^{2+} cations occupying the 12-fold coordination site between corner-sharing $Mn^{4+}O_6$ octahedra. At moderate temperatures, $SrMnO_3$ forms a hexagonal 4H structure (sp. gr. $P6_3/mmc$, a = 5.454(1) Å, c = 9.092(2) Å, $Z = 4$),[9] and at high pressures and high temperatures (6 GPa and 1773 K) a 6H structure (sp. gr. $P6_3/mmc$, a = 5.42892(1) Å, c = 13.4025(3) Å, V = 342.0929(9) Å³, $Z = 6$) is formed.[8,10] The 4H- and 6H-variants of $SrMnO_3$ form face-sharing octahedral dimers and pairs of corner-sharing MnO_6 octahedra in the periodic sequence of *hchc* and *cchcch*, respectively, where *c* and *h* denote cubic and hexagonal types of layer stacking, respectively.

The hexagonal 6H structure of $SrMnO_3$ can be stabilized at normal pressures by partial replacement of Sr or Mn by

[a] *Institute of Solid State Chemistry, Ural Branch of the Russian Academy of Sciences, 91 Pervomayskaya, Ekaterinburg, Russia*
[b] *M.N. Mikheev Institute of Metal Physics of the Ural Branch of the Russian Academy of Sciences, Ekaterinburg, Russia*
[c] *Institut Laue-Langevin, BP 156, 6, rue Jules Horowitz, Grenoble Cedex 9, France*
[d] *Department of Materials and Environmental Chemistry, Arrhenius Laboratory, Stockholm University, S-106 91 Stockholm, Sweden*
[e] *Max Planck Institute of Colloids and Interfaces, Am Mühlenberg 1, 14476 Potsdam, Germany. E-mail: nadja.tarakina@mpikg.mpg.de*
[f] *School of Engineering and Materials Science, Queen Mary University of London, Mile End, London E1 4NS, UK*
† Electronic supplementary information (ESI) available. See DOI: 10.1039/c8tc05717f

This journal is © The Royal Society of Chemistry 2019

J. Mater. Chem. C, 2019, 7, 2085–2095 | 2085

other elements. During the synthesis of the 15-layered rhombo-hedral (15R) perovskite, $SrMn_{0.9}Fe_{0.1}MnO_{3-x}$,[12,13] a 6H-layered perovskite of the same composition was found to be an inter-mediate phase. The latter phase was obtained in pure form at 1350 °C. In the $Sr_{1-x}La_xMnO_3$ solid solutions, a 6H-layered perovskite was also found to form at $x = 0.1$.[14]

The crystal structure and magnetic properties of the double perovskite Sr_2MnSbO_6 have been extensively studied.[15–19] Depending on the synthesis method, different crystal structure modifications of Sr_2MnSbO_6 can be formed. Samples prepared at low temperatures have a random distribution of Mn^{3+} and Sb^{5+} cations at the octahedral positions, resulting in the space group $I4/mcm$.[15] In ref. 17 and 18, the structure of Sr_2MnSbO_6 was described in the space group $I4/m$ with an ordered dis-tribution of cations at the octahedral positions. The presence of the Jahn–Teller cation Mn^{3+} distorts the coordination environment and contributes considerably to octahedral tilting. Accordingly,[19] this structure of Sr_2MnSbO_6 is stable in the temperature range of 2–750 K. Above 750 K, a cubic modifica-tion with space group $Fm\bar{3}m$ is formed.

The magnetic properties of $SrMn^{4+}O_3$ and $Sr_2Mn^{3+}SbO_6$ differ considerably because the latter has half of the octahedral positions occupied by diamagnetic Sb^{5+} ions. Cubic $SrMnO_3$ is antiferromagnetic with the Néel temperature $T_N = 240$ K.[8] 4H-SrMnO$_3$ also possesses antiferromagnetic properties with $T_N = 280$ K,[20] and short-range antiferromagnetic interactions are retained in the paramagnetic region. The magnetic proper-ties of 6H-SrMnO$_3$ are expected to be defined by Mn–Mn inter- and intradimer interactions, and the temperature dependence of the magnetic susceptibility by the dimeric behaviour. How-ever, in ref. 8 it was established that the temperature depen-dence of the magnetic susceptibility $\chi(T)$ for 6H-SrMnO$_3$ is typical of a three-dimensional antiferromagnetic compound with a maximum at $T_N = 235$ K. The magnetic susceptibility of 6H-SrMnO$_3$ above T_N follows the Curie–Weiss law with a Curie–Weiss constant θ of $-743(3)$ K and an effective magnetic moment μ_{eff} of 4.099(6) μ_B (the theoretical value μ_{theor} for the Mn^{4+} cation is 3.873 μ_B). The ratio $\theta/T_N = 3.2$ is indicative of the presence of frustration. The magnetization *vs.* magnetic field curves are linear up to 10 kOe, and there are upturn deviations from the linear behaviour for higher magnetic fields.

The magnetic susceptibility of Sr_2MnSbO_6 exhibits a divergence between field cooling (FC) and zero field cooling (ZFC) curves at 25 K[18] and nonequilibrium dynamics and memory at low temperatures.[19] No long-range magnetic ordering was found at 2 K. It is believed that Sr_2MnSbO_6 reaches an unconventional spin-glass state at low temperatures. The magnetization *vs.* magnetic field dependence at 5 K displays a Brillouin-like curvature with a hysteresis loop. The Curie–Weiss law $\chi = C/(T - \theta)$ is fulfilled only in the temperature range of 300–400 K with a positive Weiss constant. The experimental value of μ_{eff} (5.68 μ_B) is significantly higher than the calculated value $\mu_{cal} = 4.90$ μ_B for Mn^{3+}. These results show that the magnetic behaviour of Sr_2MnSbO_6 is determined by weak cluster-type ferromagnetic interactions.[18] The reasons for the lack of magnetic ordering in Sr_2MnSbO_6 are not yet completely clear.

However, magnetic ordering of B-site cations in Sr_2MnSbO_6-based compounds is possible to realise through heterovalent substitution of Sr^{2+} by La^{3+}.[21] The then obtained $SrLaMnSbO_6$ has a monoclinically distorted double-perovskite structure with ordered Mn^{2+} and Sb^{5+} cations and shows long-range anti-ferromagnetic (AFM) ordering below $T_N = 10$ K and significant ferromagnetic correlation below 90 K. At the same time, it has been shown that the magnetic properties of the rhombohedral perovskite $La_{0.67}Ba_{0.33}Mn_{1-x}Sb_xO_3$ ($x = 0.01$, 0.03 and 0.07) can be modified by varying the Sb doping.[22] A small increase of the Sb content changes the Mn^{3+}/Mn^{4+} ratio and thus influences the double exchange interactions and leads to a decrease in the Curie temperature (T_C) from 326 to 296 K.[22]

The above data motivated us to examine systems based on $SrMn^{4+}O_3$ and $Sr_2Mn^{3+}SbO_6$ manganites to identify the struc-tural and magnetic properties of compounds and/or solid solutions with mixed manganese oxidation states Mn^{3+}/Mn^{4+}. The wide variety of properties of manganites is determined not only by the differences in chemical composition, but also by the differences in their structure, in particular the disordered or ordered arrangement of B-site cations (Mn and Sb) at octahedral positions. The aim of this study was to find out how the structure of substituted manganites $SrMn_{1-x}Sb_xO_3$ with a mixed oxidation state of manganese, Mn^{4+}/Mn^{3+}, affects their magnetic characteristics.

Experimental

$SrCO_3$ (99.95%), Mn_2O_3 (99.95%) and Sb_2O_3 (99.95%) were used as the initial compounds for the synthesis of $SrMnO_3$–Sr_2MnSbO_6 solid solutions. Mixtures of initial reagents were pressed into pellets and calcined in air at 950 °C for 30 h and at 1150 °C, 1250 °C and 1350 °C for 12 h with intermediate cooling and regrinding in an agate mortar.

The purity of the synthesized product was checked using X-ray powder diffraction (XRPD). XRPD patterns were collected at room temperature on a XRD Shimadzu 7000S diffractometer using Cu Kα radiation. The possible impurity phases were checked by comparing their XRPD patterns with those in the PDF2 database (ICDD, USA, Release 2016). For the crystal structure refinements, XRPD patterns were collected on a STADI-P (Stoe) diffractometer in transmission geometry with a linear mini-PSD detector, using Cu Kα$_1$ radiation in the 2θ range 5° to 120° with a step of 0.02°. Polycrystalline silicon (a = 5.43075(5) Å) was used as an external standard.

The microstructure and chemical composition of obtained samples were analysed using a JEOL JSM-5900 LV microscope equipped with a JEOL energy-dispersive X-ray detector (EDX).

Neutron powder diffraction patterns (NPD) were collected at the ILL facility at Grenoble (France) using the D2B high-resolution two-axis diffractometer ($\lambda = 1.594$ Å) equipped with a cryofurnace, which enables to perform measurements at temperatures in the range of 2–500 K. For all measurements, the samples were placed in a vanadium cylinder with a diameter of 8 mm.

The crystal structure refinement was carried out with the GSAS[23,24] program suite using the NPD data for low and high

2086 | *J. Mater. Chem. C*, 2019, **7**, 2085–2095

This journal is © The Royal Society of Chemistry 2019

temperatures and a combination of XRPD and NPD data for room temperature. The peak profiles were fitted with a pseudo-Voigt function, $I(2\theta) = x \times L(2\theta) + (1 - x) \times G(2\theta)$ (where L and G are the Lorentzian and Gaussian part, respectively). The angular dependence of the peak width was described by the relation $(\text{FWHM})^2 = U\text{tg}^2\theta + V\text{tg}\theta + W$, where FWHM is the full line width at half maximum. The background level was described by a combination of thirty-sixth-order Chebyshev polynomials. The absorption correction function for a flat plate sample in transmission geometry has been applied. Since neutron scattering lengths for Mn and Sb are -3.73 and 5.57 fm, respectively, the resulting scattering length of the mixed sites with Mn/Sb ratios equal to $0.667/0.333$ would be $-3.73 \times 2/3 + 5.57 \times 1/3 = -0.63$ fm, as close to zero as the value of -0.3824 fm tabulated for vanadium which is considered as transparent for low energy neutrons and used as a material for the capillary for neutron diffraction data collection. In this regard, we have fixed the Mn/Sb ratios to $0.667/0.333$ and set the values of the thermal motions to 0.025 for this site for all full-profile refinements of the $SrMn_{0.665}Sb_{0.335}O_3$ structure based on neutron data only, namely for the temperatures of 5 K and 500 K. In the analysis of the low-temperature NPD data, a two-phase refinement for every temperature was performed. In each case, the crystal structure was refined taking as starting parameters those obtained at room temperature. The magnetic structure was refined as an independent phase with the $P1$ space group for which only magnetic atoms were defined. The scale, atomic coordinates and displacement parameters were constrained for both the nuclear and magnetic structures. The bond valence sums (BVS) were calculated using the VaList program by Wills[25] according to equations given by Brown and Altermatt[26] and the bond-valence parameters, r_0 and b, tabulated by Brese and O'Keeffe.[27]

A scanning transmission electron microscopy (STEM) study was performed using a FEI (S)TEM Titan 80-300 microscope, operated at 300 kV. For the STEM study an ethanol suspension of the sample was prepared and kept in an ultrasonic bath for 5 minutes; then a drop of this suspension was put onto a holey carbon film supported on a Cu grid. High-temperature transmission electron microscopy investigations were performed using a double-tilt heating holder (Gatan model 652) on a JEOL 2100 transmission electron microscope. The selected-area electron diffraction (SAED) patterns were recorded on a Gatan Orius 200D camera.

Magnetic measurements were performed on a SQUID magnetometer MPMS-XL-5 produced by QUANTUM DESIGN.[30] The temperature was varied from 5 K to 400 K. The controlled magnetic field strength H was set to 0.5 kOe. Measurements were carried out when a specimen was cooled in zero and controlled (ZFC and FC) magnetic field. A specimen was first cooled in the zero field to 5 K, after which the magnetization (M) on heating up to 400 K (ZFC mode) was measured, followed by measurements when cooling from 400 K to 5 K (FC mode). From these measurements we found the static magnetic susceptibility $\chi = M/H$, whereas the AC susceptibility measurement technique was used to determine the real χ' and imaginary χ'' components of the dynamic susceptibility for an amplitude value of the variable magnetic field of 4 Oe and a frequency of 80 Hz.

Results and discussion

In order to obtain comprehensive information about the $SrMnO_3$–Sr_2MnSbO_6 system, we have synthesized 11 samples of the general formula $SrMn_{1-x}Sb_xO_3$ with $x = 0.025$, 0.05, 0.075, 0.10, 0.125, 0.165, 0.20, 0.25, 0.335 and 0.415. This integrated formula was used for a more convenient comparison of the compositions of the solid solutions formed on the basis of $SrMnO_3$ and Sr_2MnSbO_6.

A preliminary analysis of the XRPD patterns of the obtained solid solutions $SrMn_{1-x}Sb_xO_3$ ($x = 0.025$–0.415) collected at room temperature indicates a morphotropic transition with a variation in the antimony content. Fig. 1 and Table S1 (ESI†) show three regions: (1) $x = 0.025$–0.09, where the monoclinically distorted 6H-perovskite structure[8,29] is stable, (2) $x = 0.17$–~ 0.45, where the solid solution adopts a tetragonal double perovskite structure,[15–19] and the (1 + 2) two-phase region, where the limiting compositions of each modification coexist, with a change in Sb-content only the mass fractions of each modification change.

The unit cell parameters and volumes for both monoclinic and tetragonal modifications obey Vegard's law. For a detailed study of the crystal and magnetic structures, low and high temperature NPD data have been collected for four single phases and well-crystallized samples of $SrMn_{1-x}Sb_xO_3$ with $x = 0.075$, 0.20, 0.335 and 0.415.

Crystal structures of $SrMn_{1-x}Sb_xO_3$ solid solutions

Monoclinic solid solutions. As seen in Table S1 (ESI†), all the lattice parameters and the unit cell volumes increase within the monoclinically distorted 6H solid solution as a result of Sb-for-Mn substitution, which is due to a reduction of the
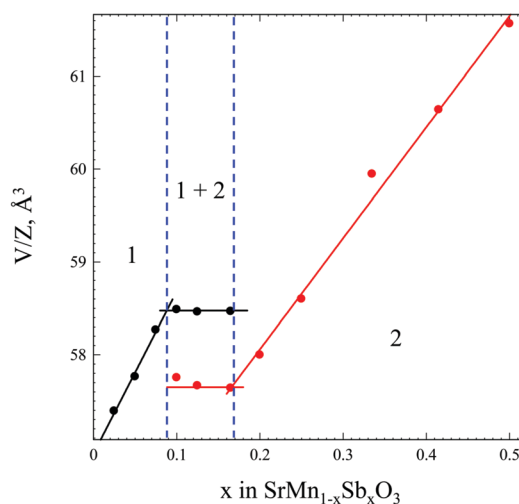

Fig. 1 Dependence of formula unit volume V/Z on antimony content for $SrMn_{1-x}Sb_xO_3$ ($x = 0.025$–0.415). Three regions can be distinguished: (1) $x = 0.025$–0.09 where the monoclinic modification ($C2/c$) is stable and (2) $x = 0.17$–0.415, tetragonal modification ($I4/mcm$), and (1 + 2) where mixtures with various ratios of these two modifications exist.

This journal is © The Royal Society of Chemistry 2019

J. Mater. Chem. C, 2019, 7, 2085–2095 | **2087**

average oxidation state of manganese and a larger size of both Mn^{3+} and Sb^{5+} cations as compared with Mn^{4+}. All diffraction patterns of $SrMn_{0.925}Sb_{0.075}O_3$ collected in the temperature range of 1.5–500 K have been indexed in a monoclinic unit cell with the space group $C2/c$ (#15) (Table 1). The obtained lattice parameters increase with temperature, whereas the monoclinic angle decreases (Fig. 2a), which means that the degree of monoclinic distortion decreases when heated. The crystal structure of $SrMn_{0.925}Sb_{0.075}O_3$ (Table 1) has been shown to possess a monoclinically distorted 6H-perovskite structure (Fig. 3) consisting of corner-sharing octahedra around sites 4a randomly occupied by manganese and antimony ions in the ratio 0.775/0.225 and face-sharing octahedra around sites 8f occupied by manganese ions (Fig. 3a and c).

Strontium ions in sites 4e and 8f, respectively, center two polyhedra 12-fold coordinated by oxygen ions. Linear and volume thermal expansion coefficients (Table 1) are expressed by

$$\alpha_L = \frac{1}{L}\frac{dL}{dT} \text{ and } \alpha_V = \frac{1}{V}\frac{dV}{dT}, \qquad (1)$$

respectively, where L and V are unit cell parameters and volume, respectively, and dL/dT and dV/dT are their rates of change with temperature. Note that neither lattice parameters nor volume vary linearly. Therefore, the calculated values are just the average between two temperatures and are not true values at a given temperature. However, they allow us to estimate the order of magnitude and the trend in change of thermal expansion.

Table 1 Structural data for $SrMn_{1-x}Sb_xO_3$ for $x = 0.075$

			T = 1.5 K NPD	T = 80 K NPD		T = 298 K XRPD + NPD	T = 500 K NPD
Space group, #, Z			$C2/c$, 15, 12	$C2/c$, 15, 12		$C2/c$, 15, 12	$C2/c$, 15, 12
Cell constants							
a, Å			5.4602(2)	5.4612(2)		5.46826(7)	5.4829(3)
b, Å			9.4339(2)	9.4353(2)		9.4629(1)	9.4902(5)
c, Å			13.4951(4)	13.4971(4)		13.5140(2)	13.5423(6)
β, °			90.773(2)	90.764(2)		90.6545(9)	90.555(3)
V, Å^3			695.08(4)	695.42(3)		699.24(2)	704.64(6)
Sr(1)-4e (0, y, 1/4)	Y		−0.0025(8)	−0.0009(9)		−0.0015(4)	0.0027(17)
	$U_i/U_e \times 100$		1.46(9)	1.4(1)		1.11(7)	2.34(13)
Sr(2)-8f (x, y, z)	X		0.0071(7)	0.0063(7)		0.0056(3)	0.0049(10)
	Y		0.3324(7)	0.3333(7)		0.3334(4)	0.3341(12)
	Z		0.0900(3)	0.0902(3)		0.09109(9)	0.0903(3)
	$U_i/U_e \times 100$		1.71(8)	1.67(7)		1.26(5)	2.65(10)
Mn/Sb(1)-4a (0, 0, 0)	$U_i/U_e \times 100$		1.20(6)^b	1.16(6)^b		0.66(9)	1.71(9)^b
	Fraction		0.775/0.225	0.775/0.225		0.775/0.225	0.775/0.225
Mn(2)-8f (x, y, z)	X		0.9905(9)	0.9905(9)		−0.0060(4)	−0.0040(10)
	Y		0.3334(11)	0.3345(11)		0.3307(6)	0.3290(18)
	Z		0.8422(3)	0.8429(3)		0.8427(1)	0.8426(4)
	$U_i/U_e \times 100$		1.20(7)^b	1.16(6)^b		1.55(7)	1.71(9)^b
O(1)-4e (0, y, 1/4)	Y		0.5140(8)	0.5125(9)		0.5121(8)	0.5145(19)
	$U_i/U_e \times 100$		1.7(2)	1.7(2)		0.6(2)	2.2(4)
O(2)-8f (x, y, z)	X		0.2691(11)	0.2688(11)		0.2680(12)	0.2687(20)
	Y		0.2428(6)	0.2420(6)		0.2387(6)	0.2413(9)
	Z		0.2436(4)	0.2436(4)		0.2437(4)	0.2468(5)
	$U_i/U_e \times 100$		1.7(1)	1.7(1)		1.7(1)	2.2(2)
O(3)-8f (x, y, z)	X		0.0303(14)	0.0298(14)		0.0272(15)	0.0146(33)
	Y		0.8340(7)	0.8348(7)		0.8350(7)	0.8347(11)
	Z		0.0824(5)	0.0821(5)		0.0825(5)	0.0819(9)
	$U_i/U_e \times 100$		2.1(2)	2.0(2)		1.0(2)	2.7(3)
O(4)-8f (x, y, z)	X		0.2719(9)	0.2731(10)		0.2702(12)	0.2603(24)
	Y		0.0833(7)	0.0836(7)		0.0844(8)	0.0841(15)
	Z		0.0716(3)	0.0718(4)		0.0742(4)	0.0761(7)
	$U_i/U_e \times 100$		1.7(1)	1.8(1)		1.5(1)	3.1(2)
O(5)-8f (x, y, z)	X		0.7761(11)	0.7768(11)		0.7688(14)	0.7690(21)
	Y		0.0834(8)	0.0832(8)		0.0818(8)	0.0835(14)
	Z		0.0913(4)	0.0916(4)		0.0893(4)	0.0886(6)
	$U_i/U_e \times 100$		1.4(1)	1.4(1)		1.5(2)	2.6(2)
wR_p, X-ray/neutron, %			—/4.46	—/4.45	—/4.72^a ... —/4.55^a	1.15/4.53	—/4.33
R_p, X-ray/neutron, %			—/3.41	—/3.39	—/3.60^a ... —/3.46^a	0.84/3.54	—/3.43
χ^2			—/1.698	—/1.691	—/1.916^a ... —/1.783^a	1.925	1.579
$R(F^2)$, X-ray/neutron, %			—/2.20	—/2.31	—/2.43^a ... —/2.41^a	2.75/2.92	—/2.76
Thermal expansion							
a_a, 10^{-6} K^{-1}				2.333		5.922	13.218
a_b, 10^{-6} K^{-1}				1.890		13.379	14.241
a_c, 10^{-6} K^{-1}				1.888		5.737	10.345
a_V, 10^{-6} K^{-1}				6.228		25.060	37.938

^{a} R-Factors obtained without taking into account the magnetic ordering. ^{b} Thermal parameters of Mn/Sb(1) and Mn(2) atoms were constrained as single variable.
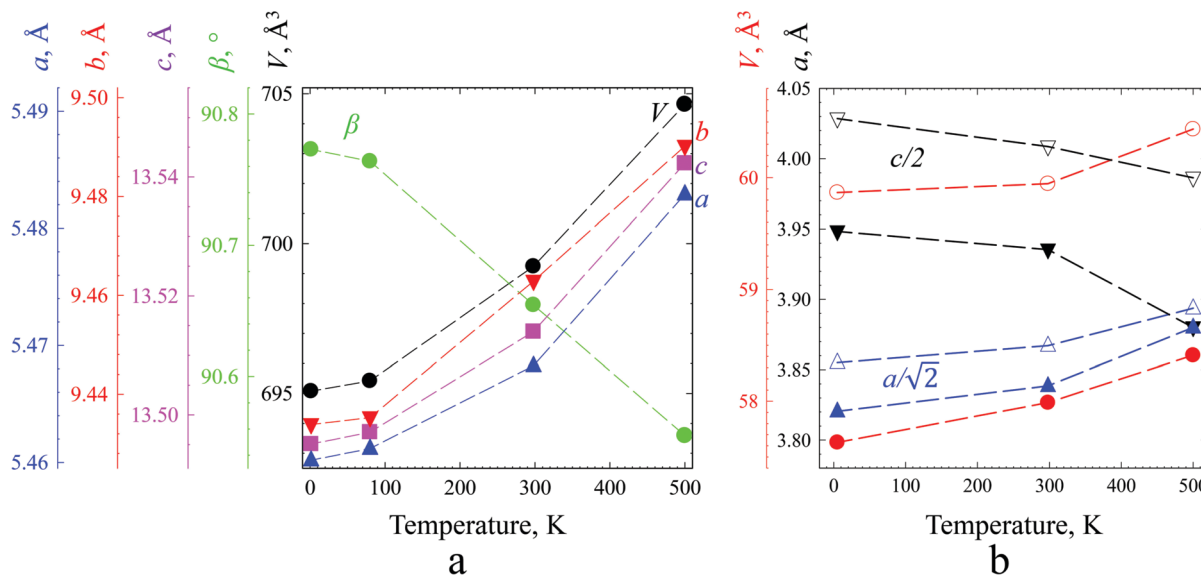
2088 | *J. Mater. Chem. C*, 2019, **7**, 2085–2095

This journal is © The Royal Society of Chemistry 2019

Fig. 2 Temperature dependence of the unit cell parameters of $SrMn_{1-x}Sb_xO_3$ (a) for $x = 0.075$ and (b) for $x = 0.20$ (filled marks) and 0.335 (unfilled marks). For clarity, in the tetragonal cell the a value has been divided by $\sqrt{2}$, the c value by 2 and V by 4 to yield a cubic cell. The estimated errors do not exceed the sizes of the marks.
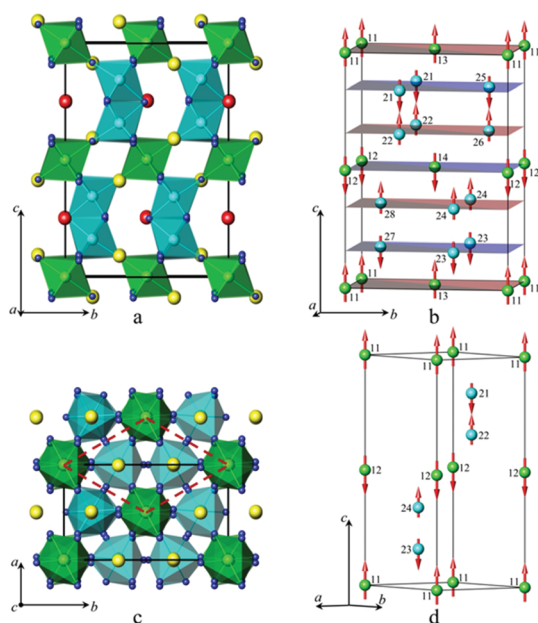

Fig. 3 Crystal structure of the monoclinically distorted 6H-perovskite $SrMn_{0.925}Sb_{0.075}O_3$, (a and c) and the arrangement of magnetic moments in monoclinic (b) and parent hexagonal lattices (d). Red, yellow, green, light blue and blue spheres indicate Sr(1), Sr(2), Mn/Sb(1), Mn(2) and O atoms, respectively. Black and red dashed lines indicate monoclinic and hexagonal unit cells. Red and blue planes in (b) indicate up and down ferromagnetically ordered planes, which alternate antiferromagnetically along the c axis.

The magnitude of the thermal expansion is small, comparable with those of iron and quartz, and anisotropy is clearly seen for the b axis at around room temperature, which is most probably a result of the rotation of polyhedra into configuration corresponding to the ideal hexagonal lattice. The oxidation state of manganese for this composition is +3.92. The calculated bond valence sum (BVS) values (Table S2, ESI†) were in good agreement with expected oxidation states, with the exception of the BVSs of Mn(1) and Sb(1), which were found to be 3.722 and 6.202, respectively, not really reflecting the expected +4 and +5 that could be explained by mixed occupation of this site.

Analysis of the selected-area electron diffraction (SAED) patterns confirmed that $SrMn_{0.925}Sb_{0.075}O_3$ crystalizes in a monoclinic unit cell with the space group $C2/c$ at room temperature.

Both HAADF-STEM images taken along the 100 direction and SAED patterns confirm the absence of planar defects or local cation ordering in the structure (Fig. 4 and Fig. S1, ESI†).

Tetragonal solid solution. Both XRPD and NPD patterns of $SrMn_{1-x}Sb_xO_3$ with $x = 0.20$, 0.335 and 0.415 collected in the temperature range of 2–500 K have been indexed with a tetragonal body-centered unit cell (Table S3, ESI†). The lattice parameter a increases with temperature, whereas c decreases (Fig. 2b), which means that the degree of tetragonal distortion is minimized when heated, and which results in a polymorphic transition at 500 K to the cubic perovskite structure type for $SrMn_{0.80}Sb_{0.20}O_3$. This transition was confirmed at the sub-micrometer scale during *in situ* heating inside the transmission electron microscope. The $h0l$ reflections with $h + l = 2n$ disappear at around 500 K, which can be explained by movement of the oxygen atoms from the general $(x, x + 1/2, 0)$ position in the tetragonal unit cell to the special $(1/2, 0, 0)$ site in the cubic unit cell (Fig. 6).

Linear and volume thermal expansion coefficients (Table S3, ESI†) calculated according to expression (1) exceed those for the monoclinic solid solutions, and the sign of the coefficient along the c axis is negative in the whole temperature range. The crystal structure of $SrMn_{1-x}Sb_xO_3$ with $x = 0.20$, 0.335 and 0.415 is

This journal is © The Royal Society of Chemistry 2019

J. Mater. Chem. C, 2019, **7**, 2085–2095 | **2089**
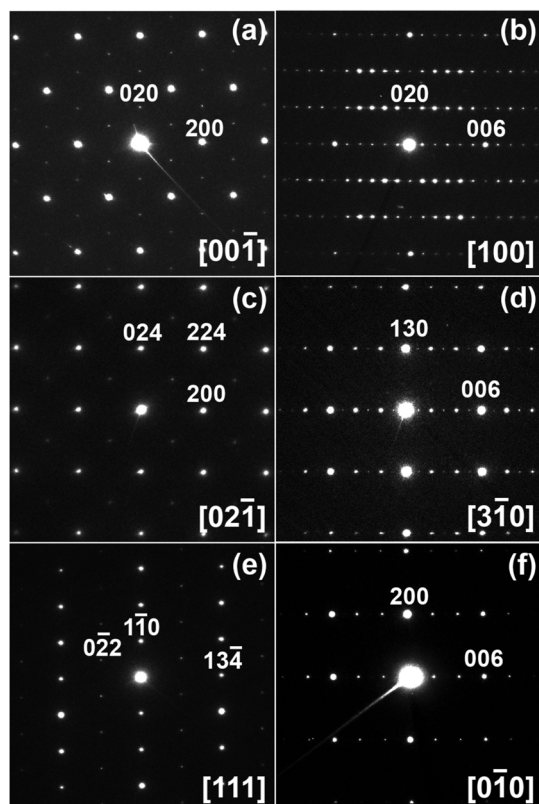
Fig. 4 SAED patterns of $SrMn_{0.925}Sb_{0.075}O_3$ taken along the main zone axes at room temperature.

described as a double perovskite with lattice parameters related to the cubic perovskite as follows: $a_t \sim a_c\sqrt{2}$ and $c_t \sim 2a_c$ and results from tilting of the octahedra ($I4/mcm - a^0a^0c^-$) (Fig. 5a).

Since there is a large amount of discussion on the ordering of manganese and antimony among octahedral positions[15–19] we tested all the proposed models and found that our synthetic route produces materials with random distribution of cations, having the highly symmetrical space group $I4/mcm$. The high-temperature modification of $SrMn_{0.80}Sb_{0.20}O_3$ observed at 500 K is also described with the highest symmetry as a cubic perovskite (Fig. 5c) with the space group $Pm\bar{3}m$ ($Pm\bar{3}m - a^0a^0a^0$) and unit cell parameter $a = 3.87998(2)$ Å, unlike the structure published for Sr_2MnSbO_6 at 900 K in ref. 19.

One should note that all full-profile refinements for all temperatures give the same R-values and quality of fit for models with and without refinement of ordering of Mn and Sb and oxygen shifts. No displacements from special sites of oxygen atoms, no ordering of manganese and antimony atoms exceeding experimental uncertainties have been detected, and the corresponding standard deviations for such parameters were much higher than those for other similar variables. These observations, along with the instability of the refinement for space groups $I4/m$ and $Fm\bar{3}m$ for the high-temperature modification usually arising from strong correlations indicate an excess in degrees of freedom and a wrong or too-low symmetry of the model.

So, we performed final refinements (Table S2, ESI†) with space groups $I4/mcm$ for $SrMn_{1-x}Sb_xO_3$ compounds with $x = 0.20$, 0.335 and 0.415 and $Pm\bar{3}m$ for the high-temperature modification with $x = 0.20$. The oxidation states of manganese for $x = 0.20$, 0.335 and 0.415 are +3.75, +3.5 and +3.29, respectively. The calculated BVS values were in good agreement with the expected oxidation states (Table S2, ESI†), except for those of Mn(1) and Sb(1) because manganese is present in two oxidation sates, +3 and +4, in addition to pentavalent antimony.
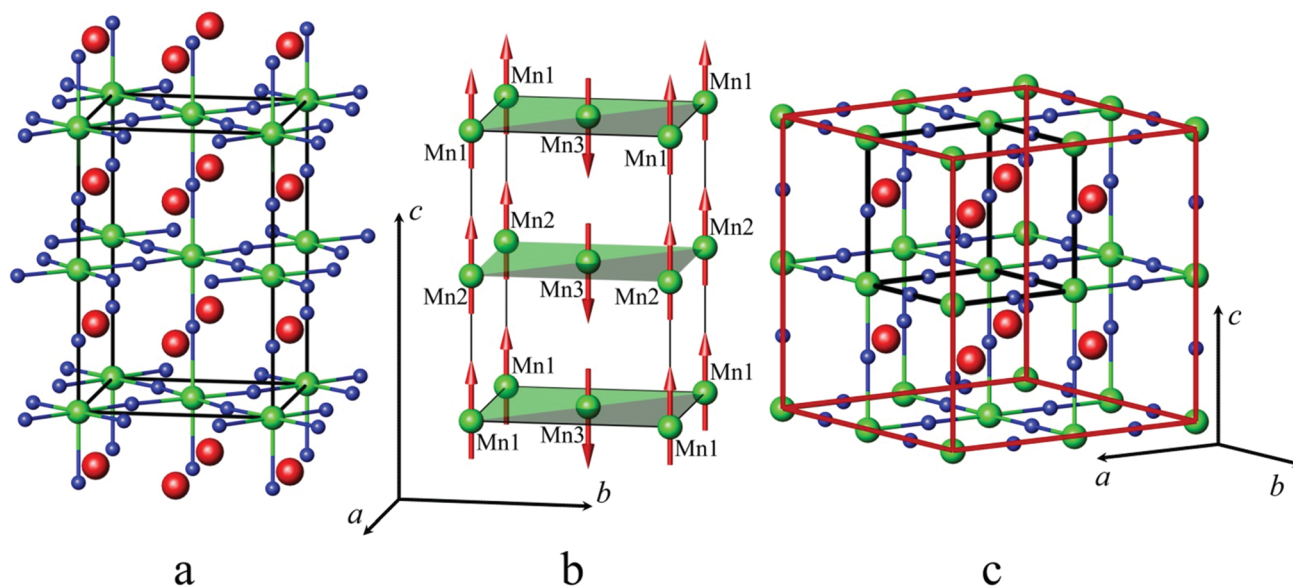

Fig. 5 Crystal structure (a) and arrangement of magnetic moments (b) of $SrMn_{0.80}Sb_{0.20}O_3$ at 5 K, and (c) cubic polymorph at 500 K. Red, green and blue spheres indicate Sr, Mn/Sb and O atoms, respectively. AFM planes ferromagnetically stacking along the c axis are show in green. Black and red lines in (c) indicate primitive and face-centered cells.
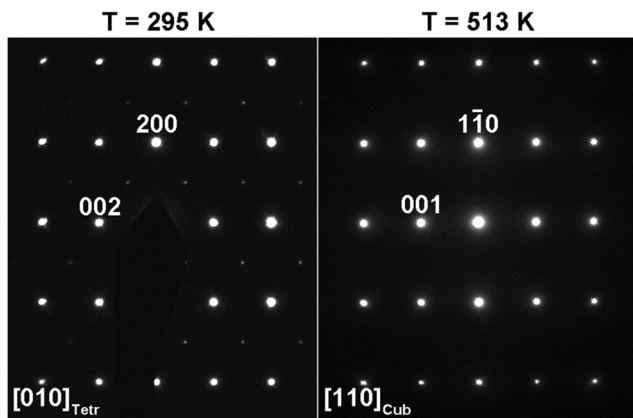
2090 | J. Mater. Chem. C, 2019, 7, 2085–2095

This journal is © The Royal Society of Chemistry 2019

Fig. 6 SAED patterns of $SrMn_{0.80}Sb_{0.20}O_3$ taken along the same direction in the crystal at room temperature and at 513 K; $h0l$ spots ($h + l = 2n$) on the $[010]_{tetr}$ diffraction pattern vanish upon heating.

Average interatomic distances (Table S4, ESI†) are in good agreement with the sums of the crystal radii according to Shannon.[28]

Mean values of Sr–O bond length vary from 2.738 Å to 2.783 Å for all solid solutions, similar to 2.729–2.738 Å in $6H$-$SrMnO_3$[8] and 2.701 Å in Sr_2MnSbO_6.[19] The sequential Mn/Sb–O distance increase of 1.930 Å, 1.939 Å, 1.964 Å and 1.973 Å for x = 0.075, 0.20, 0.335 and 0.415, respectively, reflects the growing content of Sb^{5+}, with a crystal radius of 0.74 Å, which is larger than 0.67 Å for Mn^{4+} and 0.72 Å for Mn^{3+}. The distance Mn(2)–Mn(2) in $SrMn_{0.925}Sb_{0.075}O_3$ in face-sharing octahedra is short and are 2.491(1) Å, 2.510(9) Å, 2.508(3) Å and 2.508(9) Å at 1.5 K, 80 K, 298 K and 500 K, respectively, but agrees well with 2.511(2) Å reported for the undistorted $6H$-$SrMnO_3$ polymorph.[8]

Small substitution of larger antimony for manganese in corner-sharing octahedra sites stabilizes the monoclinically distorted high-pressure modification of $SrMnO_3$. While further increase of antimony content results in a morphotropic transition, and the phase diagram contains two solid solubility regions based on monoclinic and tetragonal structures and a miscibility gap in the region from x = 0.09 to 0.17, where both modifications coexist without a change of unit cell parameters, only their mass fractions are changed.

Magnetic properties of monoclinic $SrMn_{1-x}Sb_xO_3$ (x = 0.05 and 0.075) solid solutions. The temperature dependence of the magnetic susceptibility (χ) and the AC susceptibility (χ') for $6H$-$SrMn_{0.95}Sb_{0.05}O_3$ and $SrMn_{0.925}Sb_{0.075}O_3$ measured in the ZFC and FC modes in a magnetic field of 500 Oe are presented in Fig. 7.

At high temperatures, both solid solutions are paramagnetic, and the magnetic susceptibility in the temperature range of ∼250–400 K follows the Curie–Weiss law $\chi = C/(T - \Theta)$ (Fig. 7b and d) with negative Θ values (−500 K for x = 0.05 and −368 K for x = 0.075) and μ_{exp} = 3.866 and 3.902 μ_B, respectively. These μ_{exp} values are close to μ_{theor} for the Mn^{4+} cation (electron configuration d^3, μ = 3.872 μ_B). The presence of Mn^{3+} cations with electron configuration d^4 (μ = 4.90 μ_B) led to an overestimated value of μ_{exp} for the solid solution with x = 0.075. The negative sign and the large Curie–Weiss temperatures Θ are indicative of the

presence of very strong antiferromagnetic interactions and magnetic frustration appearing due to the structural peculiarities of these perovskites. The crystal structure of $SrMn_{1-x}Sb_xO_3$ with x = 0.05 and 0.075—a monoclinically distorted $6H$-perovskite—can be considered as a two-dimensional triangular magnet,[29] in which the Mn sublattice is divided by double layers occupied by manganese and antimony ions. The presence of magnetic disorder, due to the implantation of diamagnetic cations Sb^{5+}, promotes a decrease in T_N compared with $6H$-$SrMnO_3$[8] and an abrupt growth of susceptibility when the temperature lowers (Fig. 7a and c). Similar to $4H$-$SrMnO_3$,[20] for the monoclinic solid solution $SrMn_{1-x}Sb_xO_3$ (x = 0.05 and 0.075), the short-range antiferromagnetic interactions persist in the paramagnetic region.

The $\chi(T)$ curves for the samples with x = 0.05 and 0.075 cooled in the ZFC mode and in measured field (FC mode) diverge at 190 K and ∼280 K, respectively. For $SrMn_{0.925}Sb_{0.075}O_3$, a considerable increase in χ measured in the FC mode is observed at 160 K (Fig. 7c). During further cooling of the sample, another abrupt increase in χ is observed at 41 K and a maximum at 21 K appears on the ZFC curve. The effect on the AC susceptibility at 21 K (Fig. 7d) may be an indication that at low temperature not all of the manganese cations are involved in long-range antiferromagnetic order and can form clusters that form a spin-glass state. These data suggest that the temperature vs. susceptibility dependence is determined by dimeric behavior for the monoclinic solid solution $SrMn_{1-x}Sb_xO_3$ (x = 0.05 and 0.075); in contrast to $6H$-$SrMnO_3$.[8]

The insets in Fig. 7c display the magnetization measurement results as a function of the magnetic field at 5 K. The measurements were performed during a reduction of the magnetic field from 50 kOe on samples cooled under ZFC conditions. The fact that the σ vs. H curves are nonlinear and that the magnetization does not reach saturation at 50 kOe suggest the presence of frustrated spins in the magnetic system. These results, together with the $\chi = f(T)$ data (Fig. 7a–d), may be indicative of a rather complicated model of antiferromagnetic ordering of monoclinic $SrMn_{1-x}Sb_xO_3$ solid solutions below the temperatures at which the divergence between FC and ZFC magnetic susceptibility data is observed (190 K and about 280 K for x = 0.05 and 0.075, respectively). Distinct from $6H$-$SrMnO_3$ produced at 6 GPa,[11] the $\chi(T)$ curve which displays a sharp maximum near T_N = 235 K, there is only a flat maximum near 190 K on the ZFC curve (Fig. 7a) and the $\chi' = f(T)$ curve (Fig. 7b) of the solid solution with x = 0.05.

Magnetic ordering in $SrMn_{0.925}Sb_{0.075}O_3$. The magnetic structure determination for $SrMn_{0.925}Sb_{0.075}O_3$ was performed from NPD data at 1.5 K and 80 K. An analysis of profile fits after refinement of the nuclear structure showed extra intensities for $(11\bar{1})$ at $d \approx 4.47$ Å and $(11\bar{2})$ at $d \approx 3.88$ Å (Fig. 8).

These reflections of magnetic origin can be indexed with a magnetic cell of the same dimensions and space group as the structural one, which means that we need the single propagation vector $k = (0, 0, 0)$. The magnetic symmetry analysis was performed using the program BasIreps in the FullProf suite.[31] Full details on the determination of the magnetic structure are given in the ESI† (including Tables S5–S7) and ref. 32.

This journal is © The Royal Society of Chemistry 2019

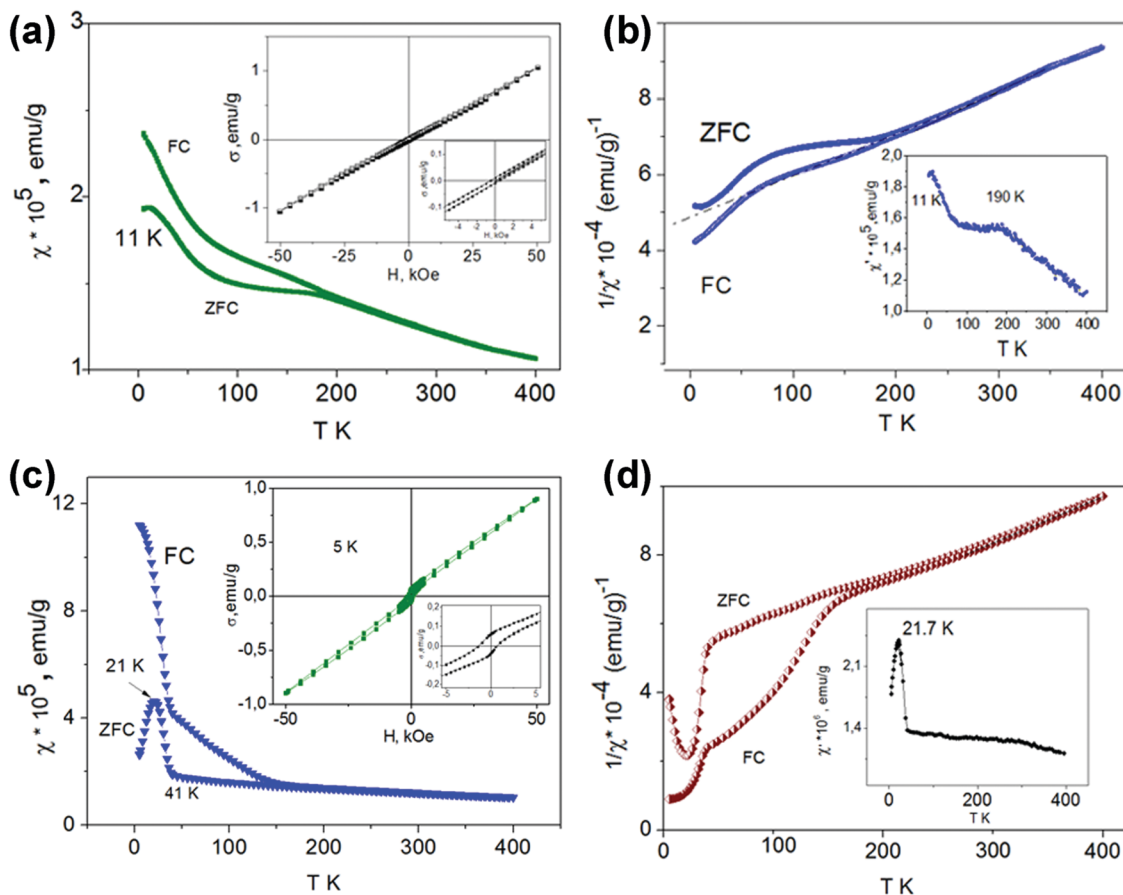*J. Mater. Chem. C*, 2019, **7**, 2085–2095 | **2091**

Fig. 7 Temperature dependence of the ZFC, and FC susceptibility in an external field of 50 kOe and field dependence of $\sigma = f(H)$ (inset) for $SrMn_{0.95}Sb_{0.05}O_3$ (a) and $SrMn_{0.925}Sb_{0.075}O_3$ (c); temperature dependence of $1/\chi$ and AC susceptibility $\chi'(T)$ (inset) for $SrMn_{0.95}Sb_{0.05}O_3$ (b) and $SrMn_{0.925}Sb_{0.075}O_3$ (d).

The relations between the cells and the arrangement of magnetic moments in monoclinic and parent hexagonal lattices are shown in Fig. 3; the difference in the fit of the NPD pattern of $SrMn_{0.925}Sb_{0.075}O_3$ at 1.5 K without taking into account the magnetic ordering and with long-range magnetic ordering is presented in Fig. 8. In general, Fourier coefficients are (u, v and w) and ($-u$, v and $-w$) and both magnetic subsystems might have antiferromagnetic spin canting in the direction of the a axis and ferromagnetic in the direction of the b axis, which means that spins are slightly tilted rather than being parallel, and a nonzero net moment is possible. In first approximation, the magnetic structure is well described as A-type antiferromagnetic, where spins are parallel to the c axis. In-plane, the coupling is ferromagnetic, while the inter-plane coupling is antiferromagnetic (Fig. 3b). The refined magnetic moments for $SrMn_{0.925}Sb_{0.075}O_3$ at 1.5 K and 80 K are presented in Table S8 (ESI†). The magnitude of the saturated moments at 1.5 K, 1.85(9) μ_B for 4a and 1.13(6) μ_B for 8f sites, respectively, is much lower than the predicted value of 2.6 μ_B for Mn^{4+} with a degree of covalency.[33] The combined populations on both sites of 92.5% of $S = 3/2$ Mn^{4+} and 7.5% of $S = 2$ Mn^{3+} ions mainly leads to antiferromagnetic interactions, although local orbital ordering of Mn^{3+} could create some ferromagnetic couplings

causing frustration. Similar long-range magnetic ordering has been reported for the 9R-type perovskite, $BaRu_{0.2}Mn_{0.8}O_3$[34] and hematite, α-Fe_2O_3,[35] below the Morin temperature. More recently, the same magnetic ordering has been published for undistorted 6H perovskite $Ba_3Fe_2TeO_9$.[36]

Magnetic properties of the tetragonal solid solution $SrMn_{1-x}Sb_xO_3$ ($x = 0.20$ and 0.335). The substitution of Mn for 33% Sb in $SrMn_{0.5}Sb_{0.5}O_3$ results in an increase in the average oxidation state of Mn from +3 to +3.5 in $SrMn_{0.665}Sb_{0.335}O_3$, which leads to a variation of the Θ constant in the Curie–Weiss law from a positive[18,19] to a negative value (-81 K) (Fig. 9a, data for χ'). The positive value of Θ is retained only above the point of the structural transition to the cubic modification (350 K). At low temperatures (Fig. 9b), the form of the $\chi = f(T)$ curve is similar to that found in ref. 18 for Sr_2MnSbO_6 and is characterized by the divergence of ZFC and FC data at 28 K in the 5 kOe magnetic field and a maximum on the ZFC dependence at 10 K. The magnetization vs. magnetic field dependence at 2 K displays a Brillouin-like curve with a very small hysteresis (inset on Fig. 9b).

The increase in the Mn content and in the average oxidation state to +3.75 in tetragonal $SrMn_{0.80}Sb_{0.20}O_3$ qualitatively changes the temperature dependence of the magnetic susceptibility (Fig. 9c). The appearance of a maximum on the $\chi = f(T)$ dependence
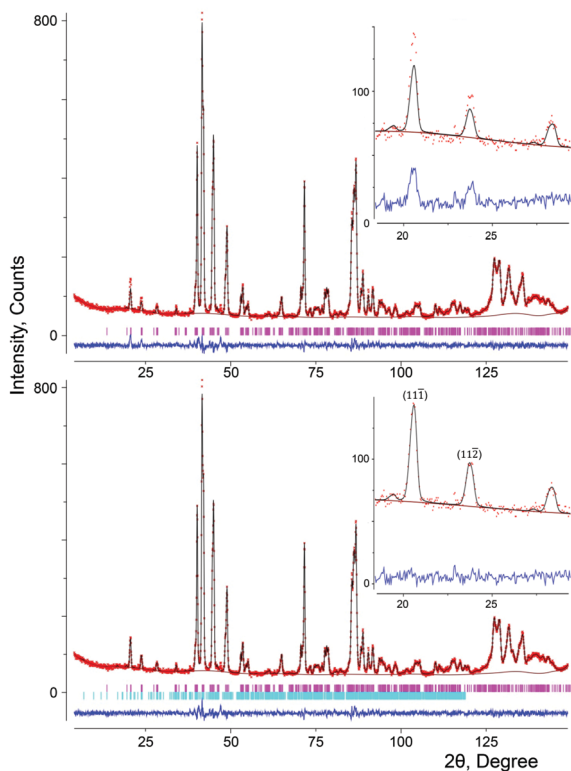
2092 | J. Mater. Chem. C, 2019, **7**, 2085–2095

This journal is © The Royal Society of Chemistry 2019

Fig. 8 Neutron powder diffraction pattern of SrMn$_{0.925}$Sb$_{0.075}$O$_3$ at 1.5 K without magnetic ordering (top) and with magnetic ordering (bottom). The red crosses are experimental points, the solid black line is the calculated profile and the vertical marks correspond to the positions of the Bragg reflections for the crystallographic (purple, first row) and magnetic (blue, second row) structures. The difference curve is plotted at the bottom of the figure.

at 248 K and a very narrow region of validity of the Curie–Weiss law on the $1/\chi = f(T)$ dependence (in the range of 250–350 K, $\Theta = 1300$ K, not shown) allow us to suppose a long-range magnetic ordering of this solid solution, with $T_N = 248$ K. The presence of a maximum at this temperature is also confirmed by the results of AC susceptibility measurements (inset on Fig. 9c). A small anomaly in the ZFC-susceptibility at 43 K may be the evidence of the magnetic transition in Mn$_3$O$_4$, which was not found by X-ray diffraction. The magnetization-field dependence does not show significant hysteresis (not shown). The transformation of this solid solution into the cubic form is also seen on the $\chi = f(T)$ curve at about 350 K.

Magnetic ordering in SrMn$_{1-x}$Sb$_x$O$_3$ (x = 0.20, 0.335). The magnetic structure determination was performed from NPD data of SrMn$_{1-x}$Sb$_x$O$_3$ (x = 0.20, 0.335) collected at 5 K. An analysis of fit profiles after refinement of the nuclear structure showed extra intensities for (100) at $d \approx 5.403$ Å, (012) at $d \approx 3.188$ Å, (120) at $d \approx 2.416$ Å and (122) at $d \approx 2.061$ Å (Fig. 10).

These reflections can be indexed with a magnetic cell of the same dimensions as the structural one, but the crystallographic unit cell is I-centered, whereas the magnetic unit cell is primitive, which means that we need the single propagation vector $k = (1, 0, 0)$. Full details on the determination of the magnetic structure is given in the ESI† (including Table S9).
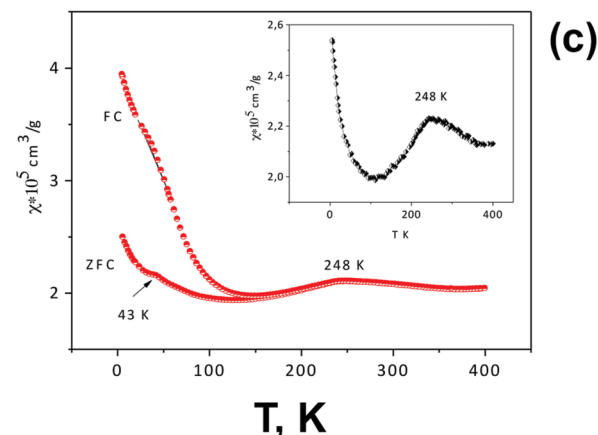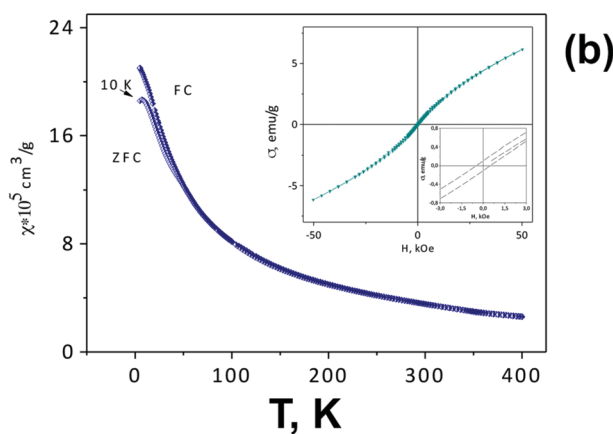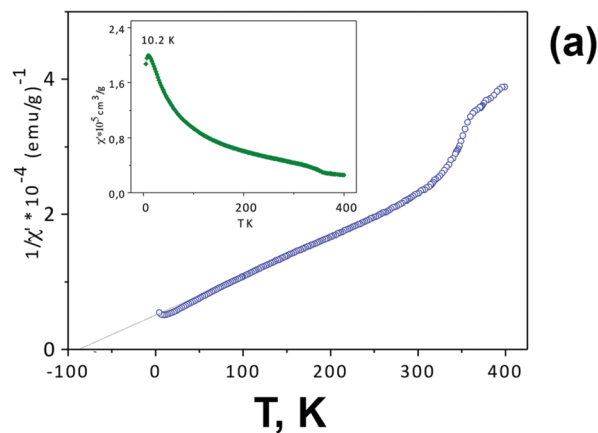

Fig. 9 (a) Temperature dependence of $1/\chi'$, AC susceptibility $\chi'(T)$ (inset) of SrMn$_{0.665}$Sb$_{0.335}$O$_3$. (b) ZFC and FC magnetic susceptibility of SrMn$_{0.665}$Sb$_{0.335}$O$_3$ measured at 0.5 kOe. The inset shows the dependence of $\sigma = f(H)$ on different magnetic fields. (c) ZFC and FC magnetic susceptibility for SrMn$_{0.80}$Sb$_{0.20}$O$_3$ measured at 0.5 kOe. The inset shows the dependence of $\chi' = f(T)$.

The refinement showed that the Γ_7 model perfectly describes the extra peaks (Fig. 10c). The magnetic structure is described as C-type antiferromagnetic, where spins are parallel to the c axis with antiferromagnetic intraplanar and ferromagnetic interplanar coupling (Fig. 5b). The refined saturated magnetic moments at 5 K, 2.79(2) μ_B and 2.00(4) μ_B for SrMn$_{1-x}$Sb$_x$O$_3$ with x = 0.20 and 0.335, respectively (Table S10, ESI†), fit well to the predicted value for Mn^{4+}, but are lower than those for Mn^{3+}.
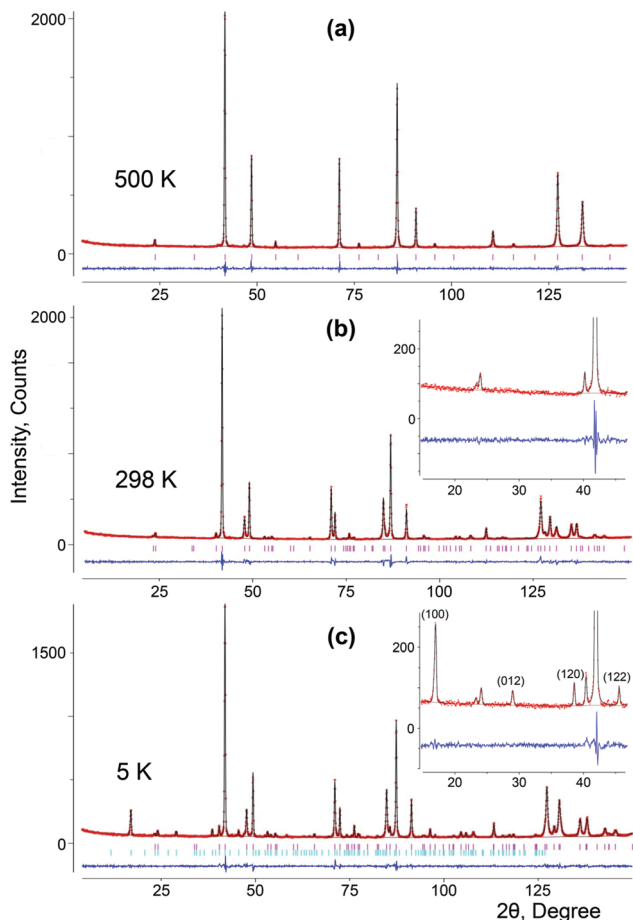
This journal is © The Royal Society of Chemistry 2019

J. Mater. Chem. C, 2019, **7**, 2085–2095 | **2093**

Fig. 10 Neutron diffraction patterns of $SrMn_{0.8}Sb_{0.2}O_3$ at 500 K (a), 298 K (b) and 5 K (c). The red crosses are the experimental points, the solid black line is the calculated profile and the vertical marks correspond to the positions of the Bragg reflections for the crystallographic (purple, first row) and magnetic (blue, second row) structures. The difference curve is plotted at the bottom of the figure.

Conclusions

Solid solutions of the $SrMn_{1−x}Sb_xO_3$ system with a perovskite structure and mixed-manganese valence Mn^{4+}/Mn^{3+} were prepared for the first time by conventional solid-state synthesis. Two ranges of solid solutions were found: (1) $SrMn_{1−x}Sb_xO_3$ ($0.025 \leq x \leq 0.09$) with a monoclinically distorted 6H-$SrMnO_3$ polytype (sp. gr. $C/2c$) and (2) $SrMn_{1−x}Sb_xO_3$ ($0.17 \leq x \leq 0.5$) with a tetragonal unit cell (sp. gr. $I4/mcm$). The crystal structure refinement was carried out using the NPD data for low and high temperatures and a combination of XRPD and NPD data for room temperature. The crystal structure of the monoclinic solid solution consists of corner-sharing octahedra around sites 4a randomly occupied by manganese and antimony ions and face-sharing octahedra around sites 8f occupied by manganese ions only. The tetragonal solid solution $SrMn_{1−x}Sb_xO_3$ has a random distribution of cations. The high-temperature modification observed at 500 K has been described with the highest symmetry: a cubic perovskite with a space group $Pm\bar{3}m$ and a unit cell parameter $a = 3.87998(2)$ Å ($x = 0.20$).

Magnetic susceptibility measurements and low-temperature NPD data show that the solid solutions adopt antiferromagnetic ordered structures. The magnetic structure of the tetragonal solid solutions $SrMn_{1−x}Sb_xO_3$ ($x = 0.20$ and 0.335) is described as C-type AFM, where spins are parallel to the c axis with AFM intraplanar and FM interplanar coupling. The refined saturated magnetic moments at 5 K, $2.79(2)$ μ_B and $2.00(4)$ μ_B for $SrMn_{1−x}Sb_xO_3$ for $x = 0.20$ and 0.335, respectively, fit well to the predicted value for Mn^{4+}, but are lower than those for Mn^{3+}. In first approximation, the magnetic structure of the monoclinic solid solution is well described as an A-type AFM, where spins are parallel to the c axis. Inside the plane, coupling is ferromagnetic while inter-plane coupling is antiferromagnetic.

Our results clearly demonstrate that antiferromagnetic order can be induced in both perovskite structures of the $SrMn_{1−x}Sb_xO_3$ system through chemical substitution. This result contradicts earlier published data for the $SrMn_{0.5}Sb_{0.5}O_3$ tetragonal perovskite in which magnetic order was not found.[18,19] The magnetic behavior of $SrMn_{0.5}Sb_{0.5}O_3$ was described by a spin-glass state with a weak ferromagnetism at low temperatures and a positive Weiss constant in the paramagnetic area indicating the presence of ferromagnetic clusters; there was no convincing explanation for the lack of a magnetic ordered state in Sr_2MnSbO_6 given so far. However, similar magnetic properties of Sr_2MnTaO_6 at low temperature[37] were explained by competing double-exchange (ferromagnetism) and super-exchange (antiferromagnetism) interactions. This conclusion was based on the assumption that Mn in this compound has a mixed oxidation state between +3 and +4. At the same time, in isostructural manganites (monoclinic Sr_2FeSbO_6 and Sr_2FeTaO_6) but with sufficient structural disorder, a partial cation ordering in the structure leads to the coexistence of a magnetically-ordered spin state and a spin-glass state.[38]

It is important that in our work, as a result of the replacement of 33% of Sb^{5+} cations by manganese in $SrMn_{0.5}Sb_{0.5}O_3$, the Weiss constant in $SrMn_{0.67}Sb_{0.33}O_3$ began to have a negative value thus pointing towards domination of AFM interactions and the formation of antiferromagnetic frustrated-spin clusters. Considering that according to our NPD data the oxygen content in the solid solutions corresponds precisely to the theoretical values, we suggest that the mean oxidation states of manganese in the solid solutions with $x = 0.33$ and 0.20 are $+3.5$ and $+3.75$, respectively. Consequently, the emergence of antiferromagnetic ordering in these solid solutions can be explained by the formation of mixed-valence manganese Mn^{3+}/Mn^{4+} states due to decrease of the diamagnetic Sb^{5+} ion content in antiferromagnetic frustrated-spin clusters.

Further substitution of Mn cations by Sb^{5+} is also a reason for the formation of the monoclinic structure with mixed-valence Mn^{3+}/Mn^{4+} states. Thus, a change in composition provokes a change in structure and magnetic properties, inducing antiferromagnetic ordering in the tetragonal ($x = 0.20$ and 0.33) and the monoclinic (at $x = 0.025$ and 0.075) solid solution based on $SrMn_{1−x}Sb_xO_3$.

This conclusion can be further supported by the analysis of results of the other works already mentioned in the introduction, in which possibilities of modification of the crystal structures

2094 | *J. Mater. Chem. C,* 2019, **7**, 2085–2095

This journal is © The Royal Society of Chemistry 2019

of manganites and their magnetic properties by chemical replacements are clearly shown.

Conflicts of interest

There are no conflicts to declare.

Acknowledgements

Notes and references

1 H. Sakai, J. Fujioka, T. Fukuda, D. Okuyama, D. Hashizume, F. Kagawa, H. Nakao, Y. Murakami, T. Arima, A. Q. R. Baron, Y. Taguchi and Y. Tokura, *Phys. Rev. Lett.*, 2011, **107**, 137601.

2 J. M. D. Coey, M. Viret and S. von Molnar, *Adv. Phys.*, 1999, **48**, 167.

3 O. Korneta, T. F. Qi, M. Ge, M. S. Parkin, L. E. De Long, P. Schlottmann and G. Cao, *J. Phys.: Condens. Matter*, 2011, **23**, 435901.

4 G. Zhang, H. Chen, Z. Gu, P. Zhang, T. Zeng and F. Huang, *Inorg. Chem.*, 2017, **56**, 10404.

5 V. G. Zubkov, G. V. Bazuev, A. P. Tyutyunnik and I. F. Berger, *J. Solid State Chem.*, 2001, **160**, 293.

6 Y. J. Choi, H. T. Yi, S. Lee, Q. Huang, V. Kiryukhin and S.-W. Cheong, *Phys. Rev. Lett.*, 2008, **100**, 047601.

7 Y. Tokura and N. Nagaosa, *Science*, 2000, **288**, 462.

8 A. A. Belik, Y. Matsushita, Y. Katsuya, M. Tanaka, T. Kolodiazhnyi, M. Isobe and E. Takayama-Muromachi, *Phys. Rev. B: Condens. Matter Mater. Phys.*, 2011, **84**, 094438.

9 B. L. Chamberland, A. W. Sleight and J. F. Weiher, *J. Solid State Chem.*, 1970, **1**, 506.

10 E. Cussen, J. Sloan, J. F. Vente, P. D. Battle and T. C. Gibb, *Inorg. Chem.*, 1998, **37**, 6071.

11 A. Kumar, A. S. Verma and S. R. Bhardwaj, *Open Appl. Phys. J.*, 2008, **1**, 11.

12 P. Lightfoot and P. D. Battle, *J. Solid State Chem.*, 1990, **89**, 174.

13 H. Kozuka, H. Yamada, T. Hishida, K. Ohbayashi and K. Koumoto, *J. Mater. Chem. A*, 2013, **1**, 3249.

14 G. Blasse, *J. Inorg. Nucl. Chem.*, 1965, **27**, 993.

15 M. W. Lufaso, P. M. Woodward and J. Goldberger, *J. Solid State Chem.*, 2004, **177**, 1651.

16 E. D. Politova, G. M. Kaleva, I. N. Danilenko, V. F. Chuprakov, S. A. Ivanov and N. Y. Venevtsev, *Izv. Akad. Nauk SSSR, Neorg. Mater.*, 1990, **26**, 2352.

17 M. Cheah, P. A. Saines and B. J. Kennedy, *J. Solid State Chem.*, 2006, **179**, 1775.

18 K. Mandal, V. V. Poltavets, M. Croft and M. Greenblatt, *J. Solid State Chem.*, 2008, **181**, 2325.

19 S. A. Ivanov, P. Nordblad, R. Tellgren and A. Hewat, *Mater. Res. Bull.*, 2009, **44**, 822.

20 P. Battle, T. C. Gibb and C. W. Jones, *J. Solid State Chem.*, 1988, **74**, 60.

21 T. K. Mandal, A. M. Abakumov, M. V. Lobanov, M. Croft, V. V. Poltavets and M. Greenblatt, *Chem. Mater.*, 2008, **20**, 4653.

22 A. Ben Hassine, A. Dhahri, L. Bouazizi, M. Oumezzine and E. K. Hlil, *Solid State Commun.*, 2016, **233**, 6.

23 B. H. Toby, *J. Appl. Crystallogr.*, 2001, **34**, 210.

24 A. C. Larson and R. B. Von Dreele, ''General Structure Analysis System (GSAS)'', Los Alamos National Laboratory Report LAUR 2004, 86-748.

25 A. S. Wills, VaList, Program available from www.ccp14.ac.uk.

26 I. D. Brown and D. Altermatt, *Acta Crystallogr., Sect. B: Struct. Sci.*, 1985, **41**, 244.

27 N. E. Brese and M. O'Keeffe, *Acta Crystallogr., Sect. B: Struct. Sci.*, 1991, **B47**, 192.

28 G. V. Bazuev and A. V. Korolyov, *J. Magn. Magn. Mater.*, 2008, **320**, 2262.

29 Y. Doi, Y. Hinatsu and K. Ohoyama, *J. Phys.: Condens. Matter*, 2009, **16**, 8923.

30 R. D. Shannon, *Acta Crystallogr., Sect. A: Cryst. Phys., Diffr., Theor. Gen. Crystallogr.*, 1976, **32**, 751.

31 FullProf, http://www.ill.eu/sites/fullprof/.

32 A. S. Wills, *J. Phys. IV France*, 2001, **11**, 133.

33 C. Yin, G. Li, W. A. Kockelmann, J. Lin and J. P. Attfield, *Phys. Rev. B: Condens. Matter Mater. Phys.*, 2009, **80**, 094420.

34 C. G. Shull, W. A. Strauser and E. O. Wollan, *Phys. Rev.*, 1951, **83**, 333.

35 F. J. Morin, *Phys. Rev.*, 1950, **78**, 819.

36 Y. Tang, R. P. Sena, M. Avdeev, P. D. Battle, J. M. Cadogan, J. Hadermann and E. C. Hunter, *J. Solid State Chem.*, 2017, **253**, 347.

37 M. Valldor, S. Esmaeilzadeh, M. Andersson and A. Morawski, *J. Magn. Magn. Mater.*, 2006, **299**, 161.

38 E. J. Cussen, J. F. Vente, P. D. Battle and T. C. Gibb, *J. Mater. Chem.*, 1997, **7**, 459–463.

This journal is © The Royal Society of Chemistry 2019

J. Mater. Chem. C, 2019, **7**, 2085–2095 | **2095**